



Denitrification characteristics and reaction mechanism of Ce-doped Fe-based catalysts from modified metallurgical dust containing iron

Zhi-fang Gao^{1,2} · Hong-ming Long^{1,2} · Xiang-peng Gao¹ · Hao Zhang¹

Received: 6 November 2023 / Revised: 1 April 2024 / Accepted: 18 April 2024
© China Iron and Steel Research Institute Group Co., Ltd. 2024

Abstract

Metallurgical dust (MD) was used as raw material to prepare rare earth Ce-doped Fe-based catalysts. The results show that the Ce_{0.1}/AMD-300 °C catalyst prepared from acid-modified diatomite (AMD) with $m_{Ce}/m_{MD} = 0.1$ (m_{Ce} and m_{MD} are the mass of Ce and MD, respectively) after being roasted at 300 °C can reach 99% NO_x removal rate in the wide temperature range of 230–430 °C and exhibits excellent SO₂ and H₂O resistance. The MD effectively removes alkali metal elements by the modification process, increases the specific surface area and optimizes the pore structure of MD. The doping of Ce element makes Fe-based catalysts have more surface adsorbed oxygen O₂ and a higher Ce³⁺/Ce⁴⁺ ratio. Through ammonia temperature-programmed desorption and hydrogen temperature-programmed reduction, it was found that the strong interaction between cerium and iron promotes the formation of more oxygen cavities in the catalyst, thereby generating more active and easily reducible oxygen species and promoting the transformation of Brønsted acid site to Lewis acid site. The research results provide a theoretical basis for the preparation of efficient and inexpensive Fe-based catalysts from MD.

Keywords Metallurgical dust · Fe-based catalyst · Denitrification · Rare earth doping

1 Introduction

Metallurgical dust (MD) is the general term for solid waste generated during sintering, ironmaking, steelmaking, and steel rolling. According to statistics, China's crude steel production was 1.03 billion tons in 2021, accounting for 53% of the total global crude steel production, and a large amount of MD was produced simultaneously, accounting for about 10% of the total steel production. Most of the MD is returned to the blast furnace as raw materials for ironmaking, which is a crude utilization of MD; however, the harmful elements like Na, K, Zn, etc., are enriched in the

blast furnace, resulting in blockage of the blast furnace and affecting the smooth operation of the blast furnace [1]. A small portion of MD is used in the construction field, such as road paving or bricks for construction, with low utilization efficiency. MD contains Fe, Al, Si, Zn, and other potential resources [2]. Rough treatment is not only easy to cause environmental pollution, but also a waste of a large number of potentially valuable resources. At present, "treating waste with waste" is one of the measures with significant energy saving and good effect on pollution control. It is a practical direction to prepare MD into adsorbent [3], flocculant [4], catalyst [5], etc., for environmental treatment, which can realize high value-added utilization of MD.

Emissions of NO_x have led to a series of serious environmental problems, including the formation of photochemical smog, acidification of soil and freshwater, and impacts on biodiversity and vegetation ecosystems [6–8]. Ammonia selective catalytic reduction (SCR) is the current mainstream flue gas denitrification process, mainly due to its mature technology, high denitrification efficiency, system stability, and no secondary pollution [6]. In the past

✉ Zhi-fang Gao
cancan20071007@163.com

✉ Hao Zhang
fengxu19821018@163.com

¹ School of Metallurgy Engineering, Anhui University of Technology, Ma'anshan 243032, Anhui, China

² Key Laboratory of Metallurgy Engineering and Resources Recycling (Anhui University of Technology), Ministry of Education, Ma'anshan 243002, Anhui, China

decades, various catalysts have been investigated for flue gas denitrification, including precious metal catalysts [9], metal oxide catalysts [10], molecular sieve catalysts [11], etc. As a commercial catalyst, V_2O_5 - WO_3 / TiO_2 catalyst can maintain a high NO_x conversion rate in the range of 300–400 °C but has poor stability in the presence of SO_2 and H_2O [12]. Therefore, the development of other economical and environmentally friendly SCR catalysts with excellent water and sulfur resistance is still a hot research topic in this field [13, 14]. Metal catalysts are of great interest because of their better water and sulfur resistance and environmental friendliness.

Considering the composition and good plasticity of MD, the synthesis of iron-based catalysts using MD is a feasible research direction [15]. MD is rich in various active components like Fe_2O_3 , Al_2O_3 , TiO_2 , etc. Among them, Fe_2O_3 has excellent oxidation ability and surface acid sites, and study has shown that the temperature range of dust iron-based catalysts can be reduced to 200–300 °C and meet the requirements of denitration activity [16]. Huangfu et al. [17] prepared iron-based catalysts from red mud, which exhibited over 80% denitration activity and good H_2O and SO_2 tolerance above 350 °C. Li et al. [18] treated the red mud catalyst by SO_2 activation method to form ferric sulfate species with more reducible Fe^{3+}/Fe^{2+} active sites to further enhance the denitration activity. Chen et al. [19] prepared red mud catalysts loaded with cerium–tungsten oxides, which produced positive interactions between cerium, tungsten, and iron oxides in red mud to promote the formation of unsaturated chemical bonds and the activation of adsorbed NH_3 species activation. It can be seen that the preparation of Fe-based SCR catalysts from MD can achieve high value-added utilization and expand the utilization pathway of metallurgical solid waste. However, due to the characteristics of high alkalinity and low specific surface area of MD, its direct use for NH_3 SCR is not satisfactory, and its modification by certain doping can improve the physical and chemical structures of the catalyst, thus enhancing the catalytic performance.

Some studies have shown that rare earth elements have strong interactions with various metal oxides. Appropriate addition of rare earth components to metal-based catalysts can effectively adjust the acidity of the catalyst surface, optimize the structure of the active center, and improve the dispersion of catalyst active components. Among them, CeO_2 has excellent redox performance and good oxygen storage and release ability and can significantly enhance the interaction between adsorbed species [20, 21]. Appropriate addition of CeO_2 can effectively prevent the sulfation of active sites, reduce the thermal stability of $(NH_4)_2SO_4$ and NH_4HSO_4 , accelerate the decomposition of $(NH_4)_2SO_4$, and improve the sulfur resistance of the catalyst [22]. At the same time, it has been reported that,

compared with the impregnation method, the sol–gel method, and the hydrothermal method, the co-precipitation method has a stronger interaction between CeO_2 and other metals oxides, which is more conducive to the high dispersion of active ingredients [23]. However, there is limited research on the preparation of iron-based catalysts using metallurgical dust containing iron as raw materials.

There have been many studies on the preparation of SCR catalysts from red mud, but there are few reports on the application of other metallurgical solid wastes in the field of SCR. In this study, the sintering machine tail ash was used as the source of active components of the catalyst, and the alkali metal elements in the MD were removed by acid hydrolysis modification to improve the physical and chemical properties of the MD. Then, the rare earth element Ce is doped by the co-precipitation method to exert the interaction between Ce and Fe, thereby improving the low-temperature denitration performance of the catalyst. To fully clarify the differences in the physicochemical properties of the catalysts, the bulk phase characteristics and physical structure of the catalysts were analyzed by X-ray diffraction (XRD), X-ray fluorescence spectroscopy (XRF), Brunauer–Emmett–Teller (BET), and scanning electron microscopy (SEM); and the surface species, surface acidity, and redox properties were analyzed by X-ray photoelectron spectroscopy (XPS), NH_3 temperature-programmed desorption (TPD), and H_2 temperature-programmed reduction (TPR). The research results can provide a preliminary theoretical basis for the preparation of novel high-efficiency low-temperature denitrification catalysts from MD containing iron, thereby achieving high value-added utilization of MD and expanding the utilization path of metallurgical iron-containing solid waste.

2 Experimental

2.1 Synthesis of catalysts

The original MD was modified by acid hydrolysis and alkali precipitation, and the rare earth element Ce was doped by co-precipitation. MD (20 g) was added into ultrapure water (500 mL), and then, a certain concentration of acid (HCl , HNO_3 or H_2SO_4) was slowly added to adjust the pH to 0, followed by stirring and heating for 4 h. After the solution was cooled to room temperature, a precipitant ($NaOH$ or $NH_3 \cdot H_2O$) was added to adjust the pH to 10. The obtained suspension was left to age for 24 h, then vacuum filtered, and washed alternately with ultrapure water and ethanol solution, and the filter cake was dried overnight. The dried sample was ground and put into a tube furnace for calcination at a heating rate of 10 °C/min to 500 °C for 4 h. The catalyst powder is compressed and crushed, and

423–635- μm particles are screened out for use. The acid-modified catalyst is named AMD, and according to the acid species, they are named as HNO_3 -AMD, HCl -AMD, and H_2SO_4 -AMD. According to the type of precipitant, they are named as NaOH -AMD and $\text{NH}_3\cdot\text{H}_2\text{O}$ -AMD.

MD (20 g) was weighed and put into ultrapure water (500 mL). Then, H_2SO_4 was slowly added to adjust pH to 0, followed by stirring and heating for 3 h. After that, a certain amount of $\text{Ce}(\text{NO}_3)_3\cdot 6\text{H}_2\text{O}$ was weighed and dissolved in ultrapure water, and then the reaction solution was added. The solution continued to be stirred and heated for another 1 h. The steps remain unchanged after that. According to the different amounts of Ce doping, they are named Ce_y/AMD ($y = m_{\text{Ce}}/m_{\text{MD}}$, where m_{Ce} and m_{MD} are the mass of Ce and MD, respectively). According to different calcination temperatures, for example, when $y = 0.1$, they are named as $\text{Ce}_{0.1}/\text{AMD}$ -300 °C, $\text{Ce}_{0.1}/\text{AMD}$ -400 °C, $\text{Ce}_{0.1}/\text{AMD}$ -500 °C, and $\text{Ce}_{0.1}/\text{AMD}$ -600 °C.

2.2 Catalyst characterization

Sample elemental composition was detected using an XRF (ARL Advan'X IntellipowerTM 3600, Thermo Fisher, USA). The phase of the samples was detected using an XRD (Ultima IV, Rigaku, Japan), and the scanning angle 2θ ranged from 10° to 80°. The specific surface area, pore volume, pore size, and other information of the sample were detected by N_2 adsorption and desorption (ASAP 2460, Mack Instruments, USA). The nitrogen adsorption–desorption isotherm was calculated by the BET equation to obtain the specific surface area, and the pore volume was calculated by the Barrett–Joyner–Halenda (BJH) model. With pore size, the samples were pretreated at 300 °C for 3 h. An SEM scanning electron microscope (NANO SEM430, FEI Corporation, USA) was used to study the surface microstructure of the samples. The elemental composition and chemical state information of the samples were detected with an XPS (K-alpha, Thermo Fisher, USA), and the charge correction was performed using the C 1s (284.80 eV) binding energy as the energy standard. The reduction ability of acid sites and reducible species on the sample surface were investigated by ammonia temperature-programmed desorption and hydrogen temperature-programmed reduction, and the test data were recorded with a thermal conductivity detector (TCD).

2.3 Catalytic performance tests

In this experiment, the fixed-bed catalytic reaction device was used for activity detection, as shown in Fig. 1. The parameters for simulating flue gas denitrification test are 500×10^{-4} vol.% NH_3 , 500×10^{-4} vol.% NO , 5 vol.% O_2 , and N_2 balance, 5 vol.% H_2O (water resistance),

50×10^{-4} vol.% SO_2 (sulfur resistance), flue gas flow of 150 mL/min, and gas hourly space velocity (GHSV) of $30,000 \text{ h}^{-1}$. Before the reaction, the impurities on the catalyst surface were removed by purging with N_2 at 100 °C for 30 min. The catalyst activity test temperature range is 130–430 °C, and the heating rate is 10 °C/min. The test results were recorded every 50 °C, and the flue gas components were analyzed using a flue gas analyzer (Ecom J2KN, Ecom Instruments GmbH, Germany). The NO_x removal rate of the catalyst is calculated according to Eq. (1).

$$\eta_{\text{NO}_x} = \left(\varphi_{[\text{NO}_x]_{\text{in}}} - \varphi_{[\text{NO}_x]_{\text{out}}} \right) / \left(\varphi_{[\text{NO}_x]_{\text{in}}} \right) \times 100\% \quad (1)$$

where η_{NO_x} represents the conversion rate of NO_x ; $\varphi_{[\text{NO}_x]_{\text{in}}}$ represents the volume fraction of NO_x at the inlet; and $\varphi_{[\text{NO}_x]_{\text{out}}}$ represents the volume fraction of NO_x at the outlet.

3 Results and discussion

3.1 MD raw material characteristics

The MD used in this experiment came from the sintering machine tail ash in Meishan Iron and Steel Group Co., Ltd., China, and its elemental composition was obtained by XRF detection. The results are shown in Table 1. The main element of MD is Fe, and the total iron (TFe) content reaches 55.64 wt.%. The MD contains a small amount of alkali metal elements including Ca, Mg, K, and other elements. Relevant studies have shown that alkali metal elements have no significant effect on the surface Lewis acid sites, but can inhibit the Brønsted acid sites, and inhibit the “fast SCR reaction” by promoting the competitive adsorption between NO and NH_3 and weakening the surface O_2 adsorption capacity. This leads to catalyst deactivation [24]. Therefore, it needs to be treated to enrich useful elements and remove harmful elements like alkali metals.

Phase analysis of MD was performed by XRD, and the results were obtained by comparing with Jade software and standard card, as shown in Fig. 2. The mineral composition in the original MD is very complex, including iron-containing phases such as magnetite (Fe_3O_4), hematite (Fe_2O_3), and siderite (FeCO_3), as well as quartz/silica (SiO_2), periclase (MgO), gibbsite ($\text{Al}(\text{OH})_3$) and other phases, and the test results are consistent with the XRF results in Table 1. In addition, there are some other components in the dust sludge as it is, but they cannot be displayed due to the low degree of crystallinity or the low content. Among them, magnetite has an inverse spinel structure, which is difficult to be effectively leached out by acid and cannot be effectively used; the rest of the quartz

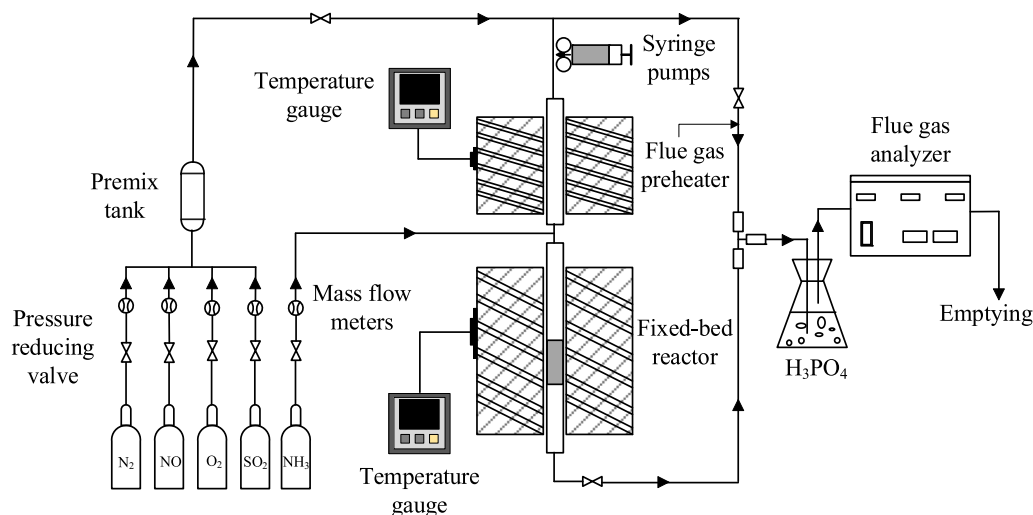


Fig. 1 Fixed-bed SCR reaction system

Table 1 Content of main element components of MD raw materials (wt.%)

TFe	Si	Ca	Al	Mg	Mn	S	K	Ti
55.64	4.11	3.26	1.48	1.36	0.26	0.29	0.15	0.10

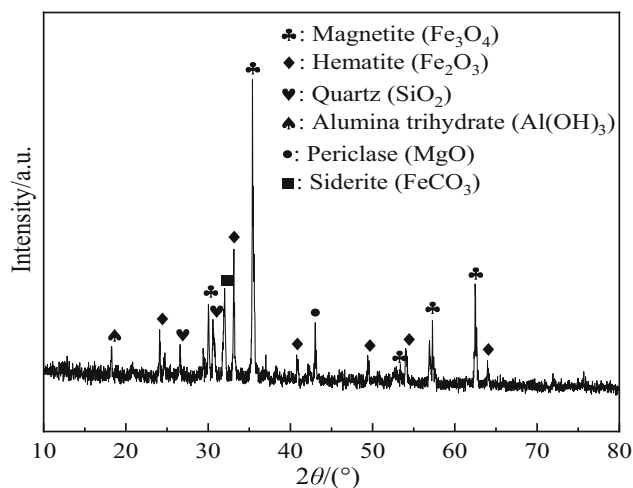


Fig. 2 XRD spectrum of MD raw materials

phase SiO_2 can exist as a catalyst carrier structure, and gibbsite ($\text{Al}(\text{OH})_3$) can be present as the active component of the catalyst.

3.2 Catalytic performance

3.2.1 Catalytic activity

It can be seen from Fig. 3 that the NO_x conversion rates of all catalysts increase first and then decrease. This is

because, as the temperature increases, the reaction rate increases and the NO_x conversion rate increases, but when the reaction temperature is too high, it will lead to oxidation and decomposition of NH_3 , which in turn reduces the NO_x conversion [25].

Figure 3a shows the NO_x conversion for AMD catalysts modified with different acids and for untreated MD catalysts. Among them, the denitration activity of the MD catalyst is poor, and the denitration rate only reaches 63% at 380 °C. After 380 °C, the denitration efficiency drops sharply to 5.8%. This is because the single iron-based catalyst has a strong oxidizing property, which makes NH_3 prone to peroxidation. After modification by acid hydrolysis, the NO_x removal rate of the MD catalyst increased significantly, with the highest point of NO_x removal rate increased by 20%–30%, and the active range moved to the low-temperature range. For the acidolyzed MD catalysts with different acid types, the order of NO_x removal rate is $\text{H}_2\text{SO}_4\text{-AMD} > \text{HNO}_3\text{-AMD} > \text{HCl-AMD}$. Previous study [26] has shown that sulfuration modification of denitration catalysts can improve the ability of catalysts to resist alkali metal poisoning, and to a certain extent, enhance the acidity of catalysts and the number of chemically adsorbed oxygen, and improve the number of acid sites and redox properties. We speculate that this may be the reason why the $\text{H}_2\text{SO}_4\text{-AMD}$ catalyst has the best denitration activity.

Figure 3b shows the NO_x conversion of AMD catalysts using different precipitants. Compared with the $\text{NH}_3\cdot\text{H}_2\text{O}$ -

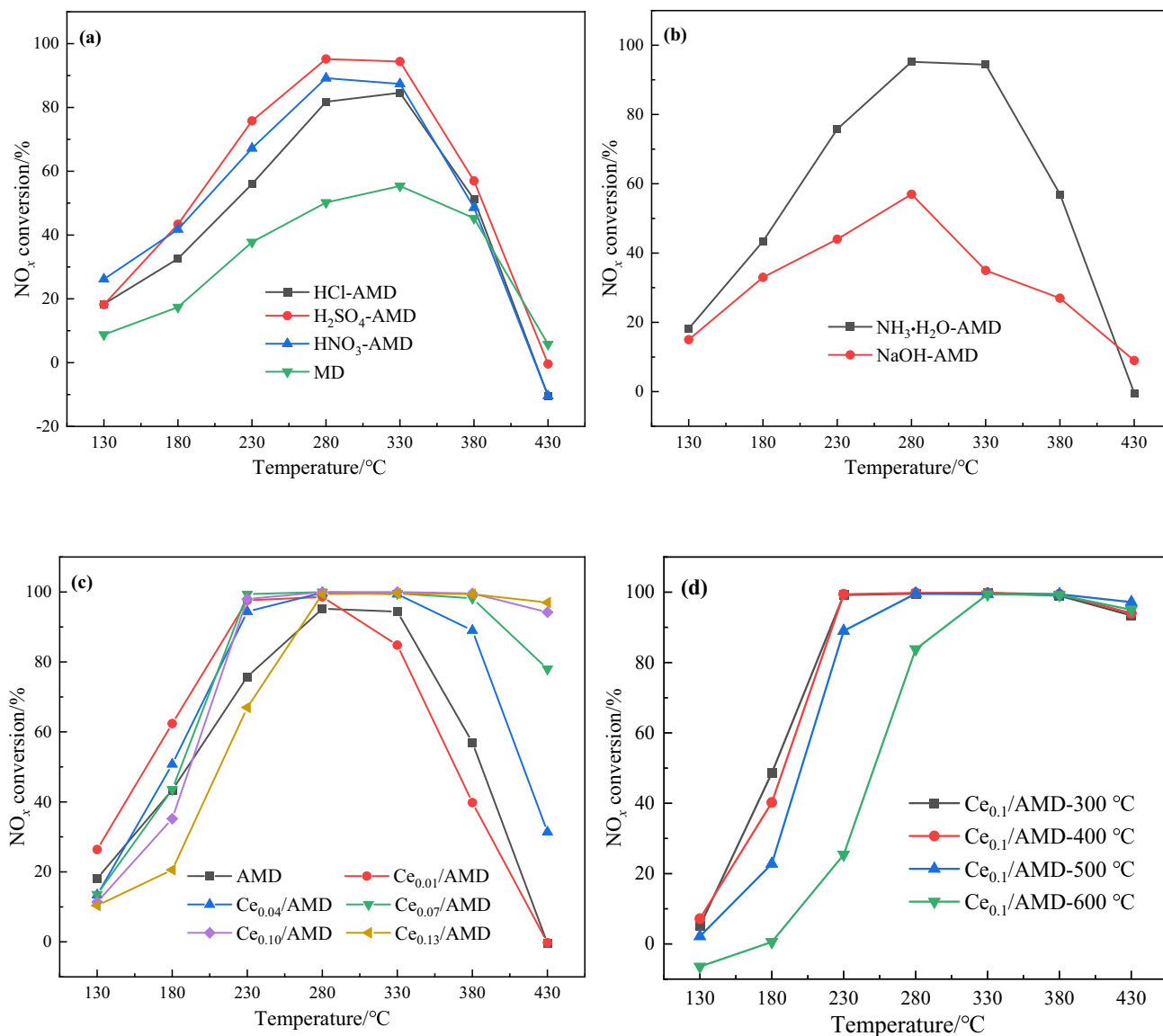


Fig. 3 NO_x conversion for catalysts with different acid types (a), precipitants (b), Ce doping (c), and calcination temperatures (d). Reaction conditions: $\varphi_{[\text{NO}]} = \varphi_{[\text{NH}_3]} = 500 \times 10^{-4}$ vol.%, $\varphi_{[\text{O}_2]} = 5$ vol.%, GHSV = 30,000 h⁻¹

AMD catalyst, the denitrification efficiency of the NaOH-AMD catalyst is lower, and the highest denitrification efficiency is 47%, which is only obtained at 280 °C. This is mainly because the NaOH-AMD catalyst cannot be washed completely, leaving too many Na ions. The residual Na ions will lead to poisoning and deactivation of the catalyst, which greatly reduces the denitrification efficiency. Compared with NaOH, using NH₃·H₂O as a precipitant can avoid the introduction of Na and K impurity ions; besides, the alkalinity of NH₃·H₂O is moderate, and the pH value range can be accurately controlled by adding slowly and repeatedly, which is conducive to the uniform precipitation of the catalyst.

Figure 3c shows the NO_x conversion of Ce_y/AMD catalysts with different Ce doping amounts. As the Ce doping amount increased from 0.01 to 0.1, the catalysts could maintain nearly 99% activity in a certain temperature range, and the temperature window gradually widened with the doping amount, Ce_{0.1}/AMD (200 °C range) > Ce_{0.07}/AMD (150 °C range) > Ce_{0.04}/AMD (100 °C range) > Ce_{0.01}/AMD (50 °C range). Observing the range of 130–230 °C, it can be found that the low-temperature activity of the catalyst is improved at low doping levels (0.01, 0.04), but with the continuous increase in the doping amount (> 0.04), the low-temperature activity of the catalyst gradually decreased. Compared with Ce_{0.1}/AMD, the NO_x conversion rate of Ce_{0.13}/AMD at high temperature

was not significantly improved. Based on the consideration of economic and denitration activity, $Ce_{0.1}/AMD$ is considered as the optimal doping catalyst, which can reach nearly 99% denitration activity in the range of 230–430 °C.

Figure 3d shows the NO_x conversion of $Ce_{0.1}/AMD$ catalysts at different calcination temperatures. It can be seen that the denitration activity of $Ce_{0.1}/AMD$ catalyst did not change much at 300 and 400 °C. With the further increase in the calcination temperature, the activity range of $Ce_{0.1}/AMD$ catalyst narrowed in the range of 130–330 °C. The denitration activity dropped sharply. Compared with the $Ce_{0.1}/AMD-300$ °C catalyst, the denitration activity of $Ce_{0.1}/AMD-600$ °C dropped from 99% to 25% at 230 °C. It can be concluded that the reasonable calcination temperature for the catalyst $Ce_{0.1}/AMD$ is 300–400 °C, and the optimal calcination temperature is 300 °C.

3.2.2 Catalyst water and sulfur resistance

Figure 4 shows the test results of the water and sulfur resistance of $Ce_{0.1}/AMD$ catalyst. When SO_2 was fed in, the denitration efficiency of $Ce_{0.1}/AMD$ catalyst dropped from 98% to about 93% within 70 min and quickly recovered to original value after disconnection, showing excellent SO_2 tolerance, which was mainly due to Fe-based catalysts having good sulfur resistance and rare earth Ce doping. Relevant studies [27, 28] have shown that the addition of Ce makes SO_2 stored in the catalyst in the form of $Ce_2(SO_4)_3$ to prevent the active components of the catalyst from being deactivated by sulfurization. The principle is shown in Fig. 5. When SO_2 and H_2O were fed at the

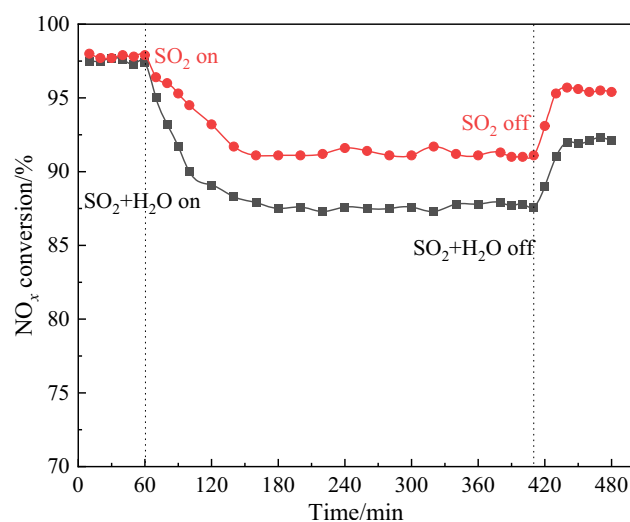


Fig. 4 Water and sulfur resistance of $Ce_{0.1}/AMD$ catalyst. Reaction conditions: $\varphi_{[NO]} = \varphi_{[NH_3]} = 500 \times 10^{-4}$ vol.%, $\varphi_{[SO_2]} = 100 \times 10^{-4}$ vol.%, $\varphi_{[H_2O]} = 5$ vol.%, $\varphi_{[O_2]} = 5$ vol.%, GHSV = $30,000 \text{ h}^{-1}$

same time, the denitration efficiency of $Ce_{0.1}/AMD$ catalyst decreased from 98% to 90% within 60 min and recovered to 95% after disconnection. It can be seen that the coexistence of SO_2 and H_2O will aggravate the occurrence of catalyst poisoning, and the permanent deactivation of the catalyst is aggravated, mainly because H_2O will promote the adsorption of SO_2 on the catalyst surface and the deposition of ammonium sulfate on the catalyst surface, thereby affecting the denitration activity.

3.3 Catalyst characterization results

3.3.1 Phase composition

The Ce_y/AMD catalyst was characterized by XRD, as shown in Fig. 6a. Through the PDF card comparison, the diffraction peaks at 24.13° , 33.12° , 35.6° , 40.8° , 49.4° , 54.0° , 57.5° , 62.4° , and 64.0° correspond to the (012), (104), (110), (113), (024), (116), (122), (214), and (300) facets (PDF#89–0596). Besides, the diffraction peak at 26.6° is the (011) crystal plane of the quartz structure (PDF#85–1053). A series of Ce-doped catalysts prepared by co-precipitation all have good crystal structures without the appearance of impurity peaks. No Ce element-related diffraction peaks are found in Fig. 6, indicating that Ce exists in the catalyst in an amorphous or highly dispersed state. Compared with the undoped catalyst, the diffraction peak intensity of the Fe species in the Ce_y/AMD catalyst is reduced, mainly because Ce interaction with Fe can improve the dispersion of the active components of the catalyst. It can be seen from Fig. 6b that with the increase in the Ce doping amount, the diffraction peak corresponding to the (104) crystal plane shifts to a smaller 2θ angle, which means that the lattice constant becomes larger, due to the doped Ce ion radius (1.034 \AA) larger than the Fe ion radius (0.645 \AA).

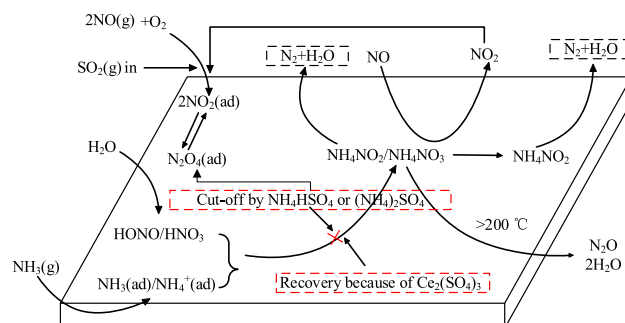


Fig. 5 Principle diagram of catalyst reaction mechanism and Ce doping anti-sulfur

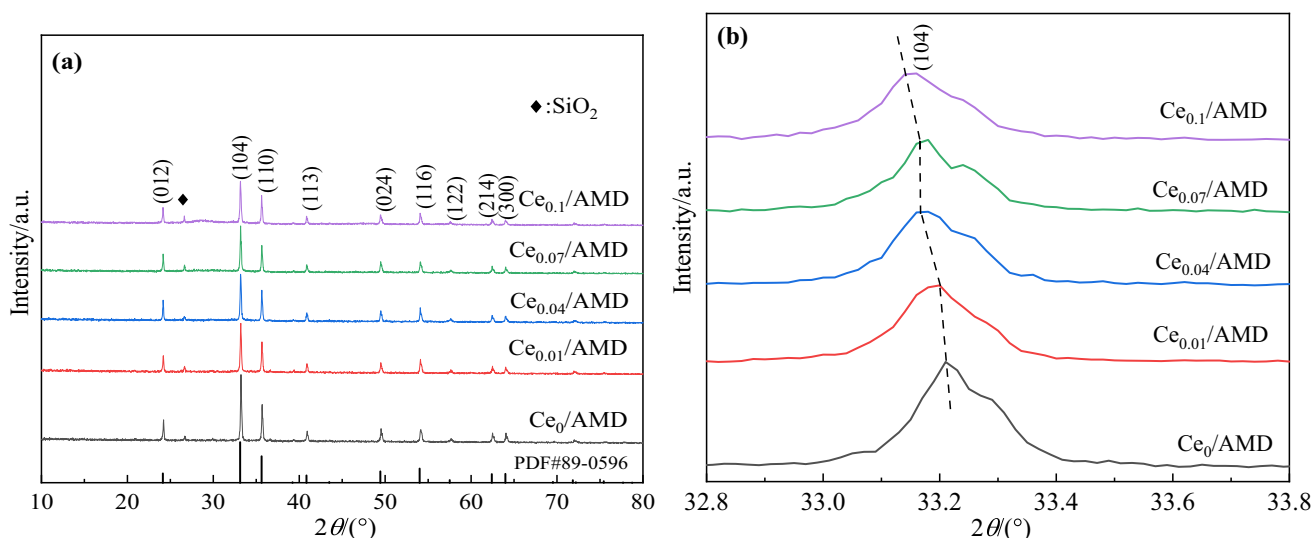


Fig. 6 XRD pattern of Ce_y/AMD ($y = 0, 0.01, 0.04, 0.07, 0.1$) catalyst (a) and comparison of (104) crystal plane diffraction peaks (b)

3.3.2 Microstructure

The microstructure images of different catalysts are shown in Fig. 7. It can be seen that the particle size distribution of the original MD is uneven, and there are many large particles in it. The surface of these large particles is smooth and there is no obvious pore structure, which is not conducive to the NH_3 SCR reaction. After the original MD catalyst was treated by acid hydrolysis, the particle size

was obviously refined, and a large number of pores were formed. The surface of the AMD catalyst doped with Ce is dominated by spherical particles, and the pore connectivity is good. The spherical particles can provide a larger specific surface area for the catalyst, which is beneficial to the adsorption of the reaction gas on its surface. With the increase in the calcination temperature, the small pores gradually collapsed, there was obvious adhesion and accumulation between particles, and the pores were

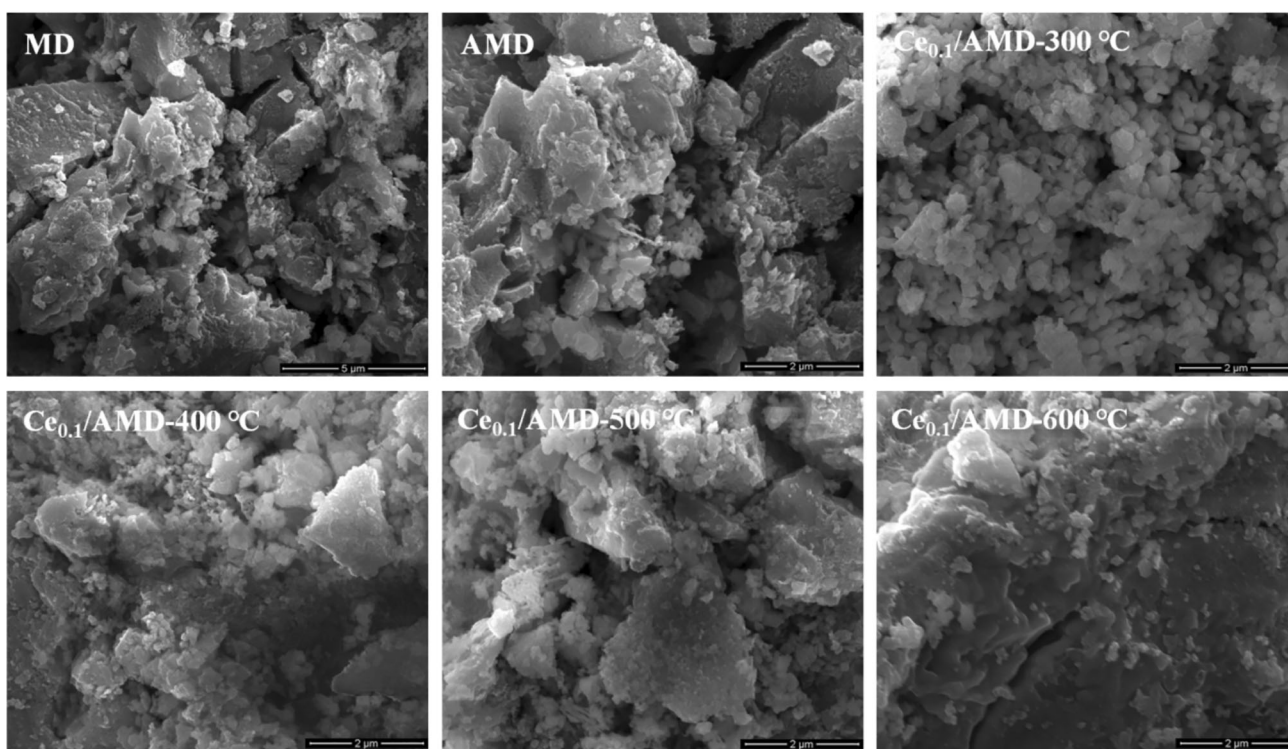


Fig. 7 SEM images of different catalysts

blocked seriously. When the calcination temperature was raised to 600 °C, the surface of the particles was in a molten state, and no obvious inter-pore channels were observed.

3.3.3 Specific surface area and pores

As shown in Table 2, the specific surface area of the MD catalyst is small, only 3.18 m²/g. After acid hydrolysis treatment, most of the alkali metals in the dust can be removed, forming more pore structures, and the specific surface area is significantly increased to 13.42 m²/g. The developed pore structure helps the gas to diffuse quickly and reach the catalyst surface to participate in the reaction. The size of the surface area can affect the number of reactive sites, thereby affecting the progress of the NH₃ SCR reaction [29]. Compared with the undoped Ce

catalyst, the iron–cerium composite catalyst has a larger specific surface area, which reflects the interaction between cerium and iron, and can improve the catalyst dispersion and refine the catalyst particle size. Combining the denitration efficiency and NH₃ TPD of AMD and Ce_{0.1}/AMD catalysts, it can be seen that the larger specific surface area is conducive to the exposure of more acidic sites, thereby significantly improving the catalytic activity [30].

As the calcination temperature increased from 300 to 600 °C, the specific surface area of Ce_{0.1}/AMD catalyst gradually decreased, which were 29.12, 24.58, 22.49, and 4.68 m²/g, respectively, and the pore size gradually expanded. The main reason is that with the increase in temperature, the pores gradually collapse, making the small pores connect large pores, and thereby reducing the specific surface area and increasing the pore size. When the temperature continued to rise to 600 °C, the specific surface area and pore volume decreased sharply, and the pore size increased significantly, mainly because the sintering phenomenon at high temperature destroyed the pore structure of the catalyst. The specific surface area of the Ce_{0.1}/AMD catalyst at different calcination temperatures is consistent with the change in the NO_x conversion rate of the Ce_{0.1}/AMD catalyst, indicating that under the same conditions, the denitrification efficiency of catalyst at different calcination temperatures is mainly affected by specific surface areas.

The N₂ adsorption and desorption curves of catalysts AMD and Ce_{0.1}/AMD are shown in Fig. 8. According to the International Union of Pure and Applied Chemistry (IUPAC) classification system, AMD and Ce_{0.1}/AMD catalysts show type II adsorption isotherms, and neither catalyst has a significant adsorption platform, indicating

Table 2 Specific surface area, pore volume, and pore size of catalysts

Catalyst	BET surface area/ (m ² g ⁻¹)	Pore volume/ (cm ³ g ⁻¹)	Pore size/ nm
MD	3.18	0.005	35.82
AMD	13.42	0.017	6.78
Ce _{0.1} /AMD- 300 °C	29.12	0.047	7.01
Ce _{0.1} /AMD- 400 °C	24.58	0.045	7.70
Ce _{0.1} /AMD- 500 °C	22.49	0.055	12.47
Ce _{0.1} /AMD- 600 °C	4.68	0.014	16.85

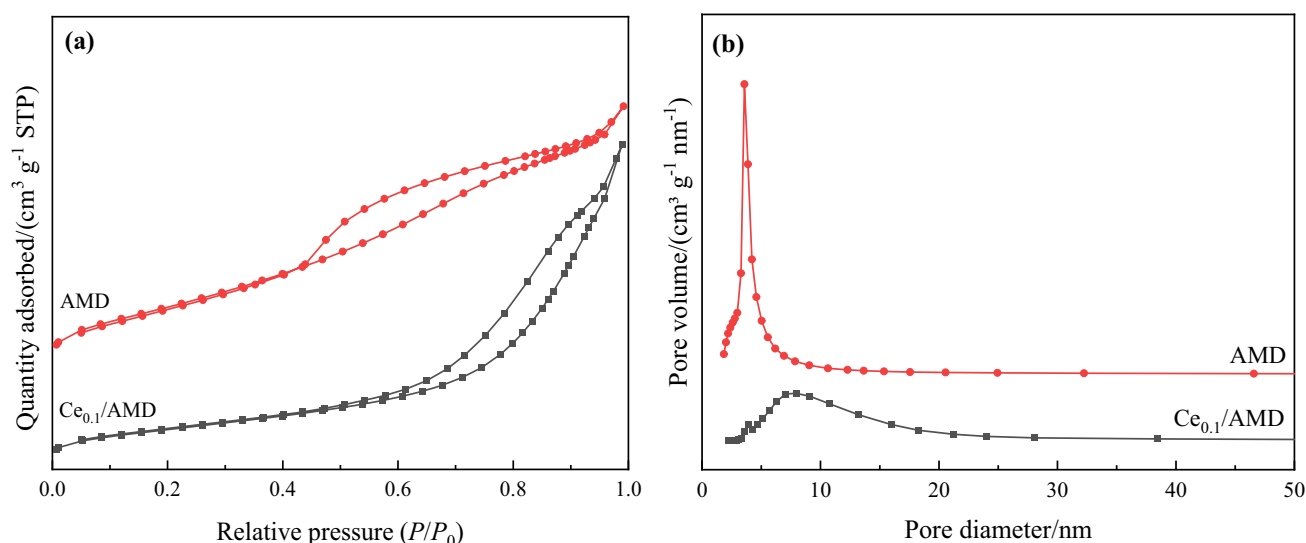


Fig. 8 N₂ adsorption and desorption curves and pore size distribution of AMD and Ce_{0.1}/AMD catalysts

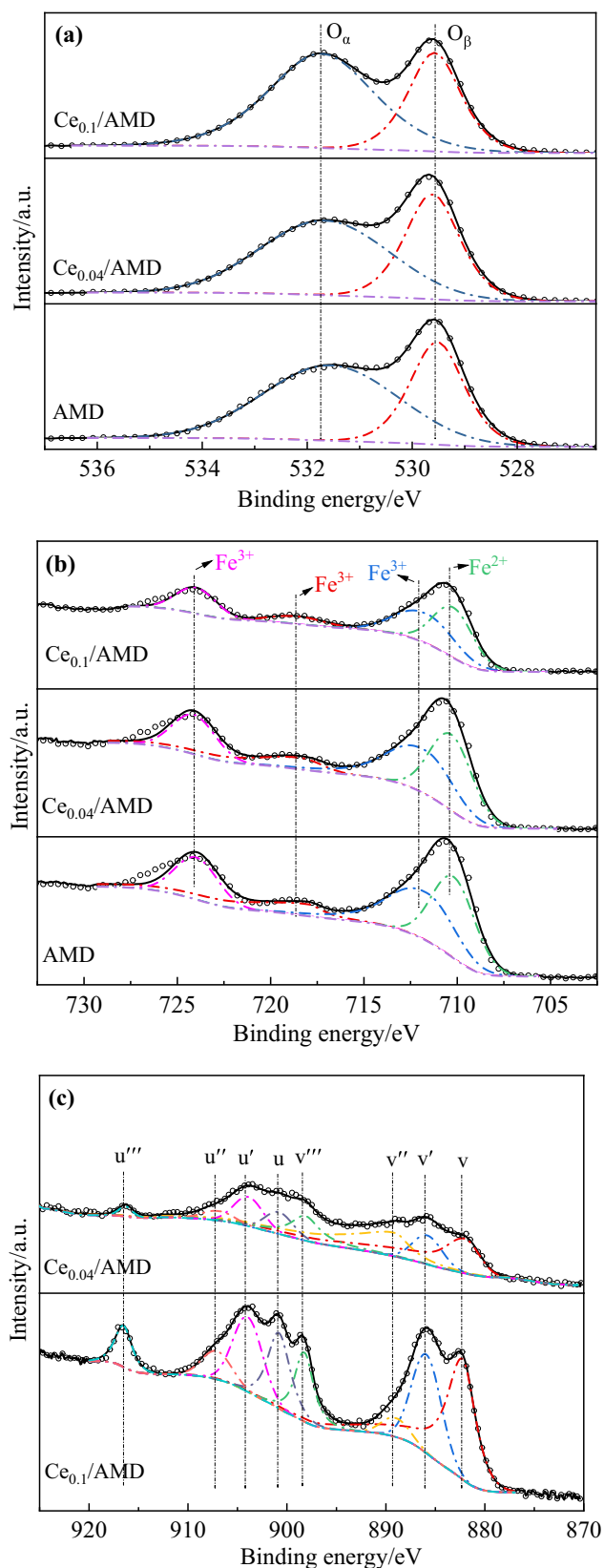


Fig. 9 XPS spectra of Ce_y/AMD ($y = 0, 0.04, 0.1$) catalysts. **a** O 1s; **b** Fe 2p; **c** Ce 3d

Table 3 Ratio of atomic concentration on different catalyst surfaces (%)

Catalyst	$O_\alpha / (O_\alpha + O_\beta)$	$Fe^{3+} / (Fe^{2+} + Fe^{3+})$	$Ce^{3+} / (Ce^{3+} + Ce^{4+})$
AMD	63.47	66.00	—
$Ce_{0.04}/AMD$	61.31	65.32	21.29
$Ce_{0.1}/AMD$	65.28	62.53	33.33

that the pore structure is relatively irregular, which is consistent with the SEM detection of the catalyst, where AMD is an H4-type hysteresis loop, and $Ce_{0.1}/AMD$ is an H3-type hysteresis loop. According to the pore size distribution diagram, the pore size of AMD catalyst is 2–10 nm, and the pore size distribution range of $Ce_{0.1}/AMD$ catalyst is 2–25 nm, which means that the doping of Ce changes the original pore structure, resulting in the increase in pore size. The main reason is that the doping amount of Ce is too large, and the Ce agglomerates on the surface of the catalyst to block the pores.

3.3.4 Surface properties

The surface elements and element valence states of AMD, $Ce_{0.04}/AMD$, and $Ce_{0.1}/AMD$ catalysts were studied by XPS, and the energy scale was corrected by using C 1s with a binding energy of 284.8 eV as the standard.

The O 1s spectrum of the catalyst is shown in Fig. 9a. It is generally believed that the binding energy in the range of 529–530 eV corresponds to lattice oxygen (denoted as O_β), and the range of 531–532 eV corresponds to surface adsorbed oxygen (denoted as O_α) [31, 32]. According to $O_\alpha / (O_\alpha + O_\beta)$, the O_α ratio was calculated, and the ratios in AMD, $Ce_{0.04}/AMD$, and $Ce_{0.1}/AMD$ catalysts were 63.47%, 61.31%, and 65.28%, respectively. It can be seen from Table 3 that the doping of a small amount of Ce can increase the amount of lattice oxygen on the surface of the catalyst. When Ce continues to be doped, O_β will be converted to O_α , which may be due to the interaction between Fe and Ce. As a result, the catalyst acquires additional surface oxygen vacancies. In the SCR reaction, O_α is more active in the oxidation process, which not only promotes the conversion of NO to NO_2 but also greatly promotes the redox cycle of the active species [33].

The Fe 2p spectrum of the catalyst is shown in Fig. 9b. Three peaks can be observed from Fig. 9b: the peak near 711, 719, and 724 eV is Fe 2p_{3/2} peak, satellite peak Fe 2p_{3/2}-sat, and Fe 2p_{1/2} peak, respectively [34]. The Fe 2p peaks of the three catalysts were divided into four peaks, and it can be seen that the Fe element in the catalysts

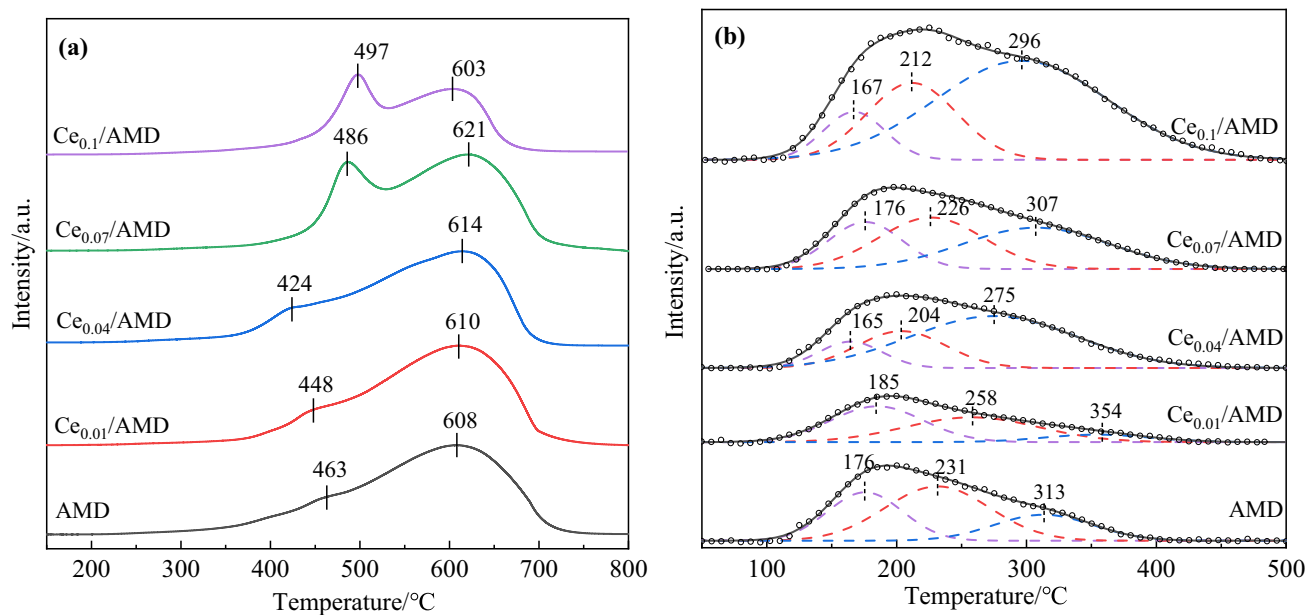


Fig. 10 H_2 TPR spectrum (a) and NH_3 TPD spectrum (b) of Ce_y/AMD ($y = 0, 0.01, 0.04, 0.07, 0.1$) catalyst

Table 4 Number of acid sites on catalyst surface

Sample	Weak acid		Middle strong acid		Sum area/a.u
	$T/^\circ\text{C}$	Area/a.u	$T/^\circ\text{C}$	Area/a.u	
AMD	176	49	231	77	161
$\text{Ce}_{0.01}/\text{AMD}$	185	45	258	45	101
$\text{Ce}_{0.04}/\text{AMD}$	165	23	204	45	185
$\text{Ce}_{0.07}/\text{AMD}$	176	47	226	74	204
$\text{Ce}_{0.1}/\text{AMD}$	167	40	212	94	367

mainly coexisted in the form of Fe^{2+} (710.2 eV) and Fe^{3+} (712, 718, 723.9 eV). The study by Devadas et al. [35] showed that the hydroxyl-bonded Fe^{3+} can provide a certain weak acid site, which is beneficial to the low-temperature catalytic activity of the catalyst. It can be seen from Table 3 that with the increase in the Ce doping amount, the Fe^{3+} ratio shows a downward trend, and some electrons in Ce are transferred. Combined with Fig. 3c, this may be the reason why the Ce_y/AMD catalyst activity decreases with the increase in Ce doping amount in the low-temperature range of 130–230 °C.

The Ce 3d spectrum of the catalyst is shown in Fig. 9c. The Ce 3d characteristic peak intensity of the $\text{Ce}_{0.04}/\text{AMD}$ catalyst is weaker than $\text{Ce}_{0.1}/\text{AMD}$, which is mainly because the $\text{Ce}_{0.04}/\text{AMD}$ catalyst is less Ce doping, resulting in a weak detection signal. Eight peaks are obtained by fitting the curve, v, v', v'', u, u', and u'' correspond to Ce^{4+} (882.0, 889.1, 898.1, 900.8, 906.8,

916.3 eV); while, v' and u' corresponds to Ce^{3+} (885.8, 903.9 eV), and it is generally believed that Ce^{3+} is in cerium–iron catalysts, because the formation of Ce^{3+} can increase oxygen vacancies and unsaturated chemical bonds, resulting in charge imbalance, which plays a crucial role in further promoting the surface adsorption of catalysts [36]. Compared with $\text{Ce}_{0.04}/\text{AMD}$, the Ce^{3+} ratio of $\text{Ce}_{0.1}/\text{AMD}$ catalyst increased to 33.33%, which shifted the redox cycle $\text{Fe}^{3+} + \text{Ce}^{3+} \leftrightarrow \text{Fe}^{2+} + \text{Ce}^{4+}$ to the left, inhibiting the formation of Fe^{3+} , consistent with the XPS results of Fe 2p.

3.3.5 Surface acidity and redox

H_2 TPR tests were performed on AMD, $\text{Ce}_{0.01}/\text{AMD}$, $\text{Ce}_{0.04}/\text{AMD}$, $\text{Ce}_{0.07}/\text{AMD}$, and $\text{Ce}_{0.1}/\text{AMD}$ catalysts, and the spectra are shown in Fig. 10a. AMD catalyst has a weak reduction peak at 463 °C, which should be

attributed to the reduction of $\text{Fe}_2\text{O}_3 \rightarrow \text{Fe}_3\text{O}_4$, and a strong reduction peak at 608 °C, and is the continuous reduction of $\text{Fe}_3\text{O}_4 \rightarrow \text{FeO} \rightarrow \text{Fe}$ [37]. When the Ce doping amount was 0.01 and 0.04, the high-temperature reduction peak remained unchanged while the low-temperature reduction peak intensity gradually increased, and the peak shifted to a lower temperature range, which was consistent with the improvement in the low-temperature activity of the catalyst in Fig. 3c. This phenomenon should be related to the formation of the iron–cerium solid solution by the catalyst. The doping of Ce makes the catalyst to form more oxygen vacancies, thereby generating more active and easily reducible oxygen species. It is worth noting that $\text{Ce}_{0.01}/\text{AMD}$ and $\text{Ce}_{0.04}/\text{AMD}$ did not show CeO_2 reduction peaks, which should be related to the low doping amount of Ce. When the Ce doping amount continued to increase to 0.07 and 0.1, a strong reduction peak appeared around 490 °C. We believe that this reduction peak corresponds to the reduction of surface Ce^{4+} to Ce^{3+} , and the reduction of Ce^{4+} and Fe^{3+} occurred at the same temperature. It is manifested as the reduction of CeO_2 , which is mainly caused by the strong interaction and co-reduction of the cerium–iron species in the catalyst [38]. For the $\text{Ce}_{0.1}/\text{AMD}$ catalyst, when the Ce element is heavily doped, the agglomeration is more serious, which is not conducive to the dispersion of surface active species, resulting in a slight decrease in the reduction peak area of the catalyst compared with $\text{Ce}_{0.07}/\text{AMD}$ and weakening the redox ability of the catalyst. The $\text{Ce}_{0.1}/\text{AMD}$ catalyst has the best activity in the case of weak redox ability, which is mainly related to the fact that the $\text{Ce}_{0.1}/\text{AMD}$ catalyst has more surface active oxygen and acid sites.

The surface acid intensity of the catalyst plays a very important role in the SCR reaction. NH_3 TPD is often used to evaluate the surface acid site distribution of catalysts. The obtained NH_3 TPD spectrum is shown in Fig. 10b. All catalysts are divided into three desorption peaks by fitting. NH_3 adsorbed on Brønsted acid sites is less thermally stable than NH_3 adsorbed on Lewis acid sites, and NH_3 desorbs at low temperatures [39, 40]. In general, the peaks before 250 °C can be attributed to the desorption of NH_3 bound to Brønsted acid and weak Lewis acid sites while the peaks after 250 °C correspond to the desorption of NH_3 bound to strong Lewis acid sites [41]. The position and area of the desorption peak represent the intensity and number of acid sites, respectively. It can be seen from Table 4 that with the increase in doping amount, the acidity intensity and the number of the catalyst both increase, and the $\text{Ce}_{0.1}/\text{AMD}$ catalyst has the most strong acid sites and total acid sites. Combined

with Fig. 3c, this is the main reason why the catalyst $\text{Ce}_{0.1}/\text{AMD}$ has the best catalytic activity.

4 Conclusions

1. Acid hydrolysis modification can remove alkali metal components in MD, enhance catalyst stability, improve tolerance to alkali metal poisoning, and optimize catalyst pore structure. Using H_2SO_4 acid hydrolysis, $\text{NH}_3 \cdot \text{H}_2\text{O}$ precipitation can achieve the best acid hydrolysis modification effect. Sulfation treatment can enhance the acidity of the catalyst and the number of chemically adsorbed oxygen and improve the number of acid sites and redox properties. $\text{NH}_3 \cdot \text{H}_2\text{O}$ has moderate alkalinity, which can avoid the introduction of impurity ions.
2. Among Ce doping modified catalysts, $\text{Ce}_{0.1}/\text{AMD}-300$ °C has the best NH_3 SCR performance, can reach 99% denitrification rate in the range of 230–430 °C, and exhibits excellent resistance to SO_2 and H_2O . The strong interaction between Ce and Fe can effectively inhibit the crystallization process of Fe_2O_3 , increase the specific surface area, and make the catalyst have more surface adsorbed oxygen O_α and a higher $\text{Ce}^{3+}/\text{Ce}^{4+}$ ratio. The formation of Ce^{3+} can increase the unsaturated chemical bonds, generate charge imbalance, and further promote the surface adsorption of the catalyst.
3. The doping of a small amount of Ce promotes the formation of more oxygen cavities in the catalyst, thereby generating more active and easily reducible oxygen species. The doping of Ce will make Ce_y/AMD generate more acidic sites, effectively enhance the NH_3 adsorption, and promote the conversion of Brønsted acid sites to Lewis acid sites. The $\text{Ce}_{0.1}/\text{AMD}$ catalyst has the strongest acid sites and total acid intensity, which is the main reason for its best catalytic activity.

Acknowledgements The research was financially sponsored by the Major Scientific Research Planning Project of Colleges and Universities in Anhui Province (Grant No. 2023AH040147), the National Natural Science Foundation of China (Grant No. 52074093), and the Outstanding Youth Scientific Research Project of Colleges and Universities in Anhui Province (Grant No. 2022AH030044).

Declarations

Conflict of interest Hong-ming Long is an editorial board member for *Journal of Iron and Steel Research International* and was not involved in the editorial review or the decision to publish this article. The authors declare that they have no conflict of interest.

References

- [1] S. Singh, A. Thakur, Mater. Today Proc. 46 (2021) 2955–2959.

- [2] S. He, L. Lin, Y.Q. Liu, Z.X. Hou, Y. Lv, W. Wu, J. Iron Steel Res. Int. 30 (2023) 697–707.
- [3] X.F. She, J.S. Wang, G. Wang, Q.G. Xue, X.X. Zhang, J. Iron Steel Res. Int. 21 (2014) 488–495.
- [4] X. Wang, N. Zhang, Y. Zhang, J. Liu, X. Xiao, K. Meng, B. Chu, C. Wang, P.K. Chu, J. Water Process. Eng. 34 (2020) 101173.
- [5] W. Shi, H. Ren, M. Li, K. Shu, Y. Xu, C. Yan, Y. Tang, Chem. Eng. J. 382 (2020) 122876.
- [6] Z. Zhang, J. Li, J. Tian, Y. Zhong, Z. Zou, R. Dong, S. Gao, W. Xu, D. Tan, Fuel Process. Technol. 230 (2022) 107213.
- [7] K. Xiao, R. Guan, J. Yang, H. Li, Z. Yu, S. Liang, W. Yu, J. Hu, H. Hou, B. Liu, Waste Manage. 85 (2019) 452–463.
- [8] Y. Xing, H. Zhang, W. Su, K. Li, J. Zhang, J. Shi, J. Tian, J. Wang, J. Clean. Prod. 289 (2021) 125756.
- [9] L. Yang, X. You, Z. Sheng, D. Ma, D. Yu, X. Xiao, S. Wang, New J. Chem. 42 (2018) 11673–11681.
- [10] S. Xie, L. Li, L. Jin, Y. Wu, H. Liu, Q. Qin, X. Wei, J. Liu, L. Dong, B. Li, Appl. Surf. Sci. 515 (2020) 146014.
- [11] B. Liu, N. Lv, C. Wang, H. Zhang, Y. Yue, J. Xu, X. Bi, X. Bao, Chin. J. Chem. Eng. 41 (2022) 329–341.
- [12] Y. Zhou, S. Ren, J. Yang, W. Liu, Z. Su, Z. Chen, M. Wang, L. Chen, J. Energy Inst. 98 (2021) 199–205.
- [13] Q. Yan, Y. Gao, Y. Li, M.A. Vasiliades, S. Chen, C. Zhang, R. Gui, Q. Wang, T. Zhu, A.M. Efstathiou, Appl. Catal. B: Environ. 255 (2019) 117749.
- [14] J. Liu, S. Zhou, H. Cheng, H. Li, W. Zhu, J. Liu, Fuel 318 (2022) 123607.
- [15] Z.F. Gao, H.M. Long, T.J. Chun, Z.J. Wu, Z.W. Yu, J. Iron Steel Res. Int. 25 (2018) 19–27.
- [16] C.G. Zhang, T.H. Chen, H.B. Liu, D. Chen, B. Xu, C.S. Qing, Appl. Surf. Sci. 457 (2018) 1116–1125.
- [17] L. Huangfu, A. Abubakar, C. Li, Y. Li, C. Wang, J. Yu, S. Gao, R. Soc. Open Sci. 6 (2019) 191183.
- [18] C. Li, H. Zeng, P. Liu, J. Yu, F. Guo, G. Xu, Z. Zhang, RSC Adv. 7 (2017) 53622–53630.
- [19] Q.Z. Chen, D. Wang, C. Gao, B. Wang, S.L. Niu, G.J. Zhao, Y. Peng, J.H. Li, C.M. Lu, J. Crittenden, Green Energy Environ. 8 (2023) 173–182.
- [20] S. Wang, Z. Chen, B. He, Z. Yan, H. Wang, L. Liu, X. Wang, Catalysts 9 (2019) 496.
- [21] Z. Xiong, Z. Li, Y. Du, C. Li, W. Lu, S. Tian, Environ. Sci. Pollut. Res. 28 (2021) 5914–5926.
- [22] N.T. Tinh, N.T.T. Van, N.P. Anh, H.K.P. Ha, N. Tri, J. Environ. Sci. Health, Part A: Toxic/Hazard. Subst. Environ. Eng. 54 (2019) 352–358.
- [23] J. Xu, H. Yu, C. Zhang, F. Guo, J. Xie, New J. Chem. 43 (2019) 3996–4007.
- [24] P. Raghunath, M.C. Lin, J. Phys. Chem. C 112 (2008) 8276–8287.
- [25] J. Liu, X. Li, Q. Zhao, J. Ke, H. Xiao, X. Lv, S. Liu, M. Tadé, S. Wang, Appl. Catal. B: Environ. 200 (2017) 297–308.
- [26] J. Zhao, Y. Yue, W. Hua, Z. Gao, Catal. Lett. 116 (2007) 27–34.
- [27] M. Peralta, V. Milt, L. Cornaglia, C. Querini, J. Catal. 242 (2006) 118–130.
- [28] R. Jin, Y. Liu, Y. Wang, W. Cen, Z. Wu, H. Wang, X. Weng, Appl. Catal. B: Environ. 148–149 (2014) 582–588.
- [29] F. Gao, X. Tang, H. Yi, J. Li, S. Zhao, J. Wang, C. Chu, C. Li, Chem. Eng. J. 317 (2017) 20–31.
- [30] J. Han, J. Meeprasert, P. Maitarad, S. Nammuangruk, L. Shi, D. Zhang, J. Phys. Chem. C 120 (2016) 1523–1533.
- [31] M.N. Khan, L. Han, P. Wang, D. Zhang, iScience 23 (2020) 101173.
- [32] T. Zhang, S. Ma, L. Chen, R. Li, X. Leng, Y. Li, F. Yuan, X. Niu, Y. Zhu, Appl. Catal. A Gen. 570 (2019) 251–261.
- [33] K. Kang, X. Yao, Y. Huang, J. Cao, J. Rong, W. Zhao, W. Luo, Y. Chen, J. Hazard. Mater. 416 (2021) 125821.
- [34] F. Liu, H. He, J. Phys. Chem. C 114 (2010) 16929–16936.
- [35] M. Devadas, O. Kröcher, M. Elsener, A. Wokaun, G. Mitrikas, N. Söger, M. Pfeifer, Y. Demel, L. Mussmann, Catal. Today 119 (2007) 137–144.
- [36] L. Yan, Y. Ji, P. Wang, C. Feng, L. Han, H. Li, T. Yan, L. Shi, D. Zhang, Environ. Sci. Technol. 54 (2020) 9132–9141.
- [37] X. Li, J. Chen, C. Lu, G. Luo, H. Yao, Fuel 294 (2021) 120552.
- [38] C. Bigey, L. Hilaire, G. Maire, J. Catal. 198 (2001) 208–222.
- [39] L. Zhang, L. Shi, L. Huang, J. Zhang, R. Gao, D. Zhang, ACS Catal. 4 (2014) 1753–1763.
- [40] R. Jin, Y. Liu, Z. Wu, H. Wang, T. Gu, Chemosphere 78 (2010) 1160–1166.
- [41] S. Chen, Q. Yan, C. Zhang, Q. Wang, Catal. Today 327 (2019) 81–89.

Springer Nature or its licensor (e.g. a society or other partner) holds exclusive rights to this article under a publishing agreement with the author(s) or other rightsholder(s); author self-archiving of the accepted manuscript version of this article is solely governed by the terms of such publishing agreement and applicable law.